Electronic Supplementary Material (ESI) for Materials Horizons.

Supplementary Information

Exchange interactions in 1*T*-VSe_2 monolayer and their modulation by electron doping via alkali metal adsorption and electride substrate

Jiawei Jiang, Rui Li, and Wenbo Mi*

Tianjin Key Laboratory of Low Dimensional Materials Physics and Preparation Technology,

School of Science, Tianjin University, Tianjin 300354, China

*Author to whom correspondence should be addressed

Email: miwenbo@tju.edu.cn

S1. Collinear magnetic states

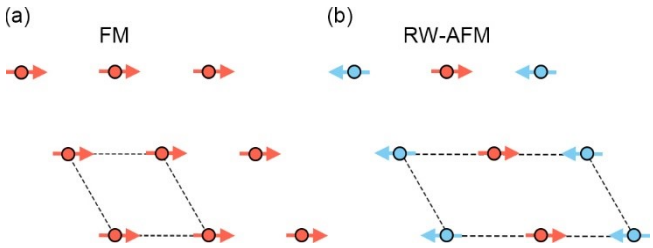

FIG. S1. (a) Ferromagnetic (FM) and (b) row-wise antiferromagnetic (RW-AFM) collinear magnetic states with the corresponding two-dimensional unit cells.

S2. Dzyaloshinskii–Moriya vectors

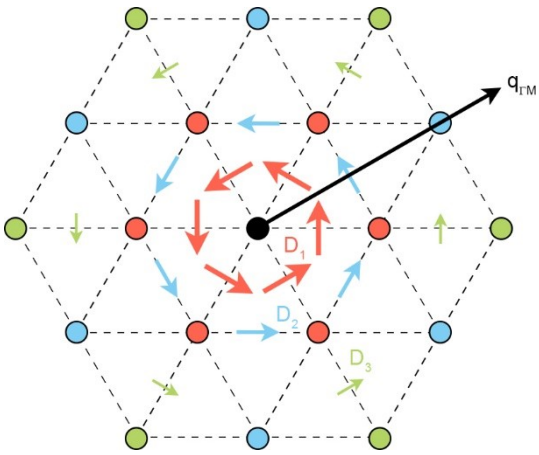

FIG. S2. Sketch of the Dzyaloshinskii–Moriya vectors for the atomic lattice of V layer from first to third neighbors (first red, second blue, third green) with the directions of the high symmetry lines of the two-dimensional Brillouin zone. The Dzyaloshinskii–Moriya vectors are perpendicular to the bond between the black reference V atom and the corresponding neighbor. The propagation direction of spin spirals for $\boldsymbol{q}$ along the Γ-M direction is shown.

S3. Higher-order exchange interactions and multi-*Q* states

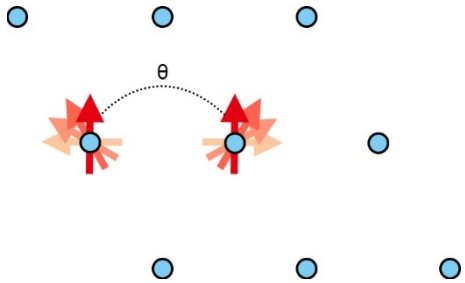

FIG. S3. Sketch of the rotation of spins at nearest neighbor sites by a relative angle θ in the angular-depended calculations.

In Fig. S4, besides the pair-wise biquadratic exchange B_{ij}, other higher-order exchange interactions including the four-site four-spin exchange K_{ijkl} and the three-site four-spin exchange Y_{ijk} can be understood as the electrons hopping between the nearest neighbors (NN) sites, and are given by[1]

$$H_{\text{4-site}} = -\sum_{ijkl} K_{ijkl}\left[\left(\boldsymbol{m}_i \cdot \boldsymbol{m}_j\right)\left(\boldsymbol{m}_k \cdot \boldsymbol{m}_l\right)+\left(\boldsymbol{m}_i \cdot \boldsymbol{m}_l\right)\left(\boldsymbol{m}_j \cdot \boldsymbol{m}_k\right)-\left(\boldsymbol{m}_i \cdot \boldsymbol{m}_k\right)\left(\boldsymbol{m}_j \cdot \boldsymbol{m}_l\right)\right], \tag{S1}$$

$$H_{\text{3-site}} = -2\sum_{ijk} Y_{ijk}\left(\boldsymbol{m}_i \cdot \boldsymbol{m}_j\right)\left(\boldsymbol{m}_j \cdot \boldsymbol{m}_k\right). \tag{S2}$$

One possibility to access the NN parameters B_1, K_1 and Y_1 is the calculation of linear combinations of multi-*Q* states, which can be energetically compared to the single-*Q* constituents. Two spin spirals Q_1 and Q_2 (Q_2=-Q_1) in the Heisenberg model are energetically degenerate. A linear combination of these two spirals will lead to a new spin configuration that is again energetically degenerate to Q_1 or Q_2 in the Heisenberg model, while this degeneracy will be lifted by considering the higher-order interaction terms. If a linear combination of Q_1 and Q_2 is formed with a phase shift of π/2 between the two spirals, a solution is obtained that again fulfills the requirement of constant *m* at all lattice sites. Here two noncollinear magnetic states are adopted: Q_1=↖↗↘↙ and Q_2=↗↖↙↘, which meet the above conditions. The linear combination of Q_1 and Q_2 is ↑ ↑ ↓ ↓

(uudd) state[2] with constant m at all sites. Since the M point is corresponding to the RW-AFM states (spin spiral wavelength λ=2a with a being the nearest-neighbor length) in the single-Q state, the uudd state will occur at q=ΓM/2 and q=3ΓK/4 (q=ΓKM/2), which are corresponding to different high symmetry paths, as shown in Fig. S5.

Similarly, in the 2D-BZ there are three M points which are equivalent in symmetry, but are different to each other with q vectors.[3] Within the Heisenberg model, the energy of each spin spiral denoted by one of three q vectors or any orthogonalized linear combination of those are degenerate, while this degeneracy will be lifted by considering the higher-order interaction terms. Thus, a linear combination state, a so-called $3Q$ state, in a 2×2 supercell with $\boldsymbol{m}_\alpha = (0,0,1)$, $\boldsymbol{m}_\beta = \left(-2\sqrt{2}/3, 0, -1/3\right)$, $\boldsymbol{m}_\gamma = \left(\sqrt{2}/3, -\sqrt{6}/3, -1/3\right)$ and $\boldsymbol{m}_\delta = \left(\sqrt{2}/3, \sqrt{6}/3, -1/3\right)$ is adopted, as shown in Fig. S5. One can calculate the B_1, K_1 and Y_1 by solving the three coupled equations below[4]:

$$\Delta E_{\mathrm{M}}^{3Q} = E_{\mathrm{M}}^{3Q} - E_{\mathrm{M}}^{1Q} = \frac{16}{3}\left(2K_1 + B_1 - Y_1\right), \tag{S3}$$

$$\Delta E_{\Gamma\mathrm{M}/2}^{2Q} = E_{\Gamma\mathrm{M}/2}^{2Q} - E_{\Gamma\mathrm{M}/2}^{1Q} = 4\left(2K_1 - B_1 - Y_1\right), \tag{S4}$$

$$\Delta E_{3\Gamma\mathrm{M}/4}^{2Q} = E_{3\Gamma\mathrm{M}/4}^{2Q} - E_{3\Gamma\mathrm{M}/4}^{1Q} = 4\left(2K_1 - B_1 + Y_1\right). \tag{S5}$$

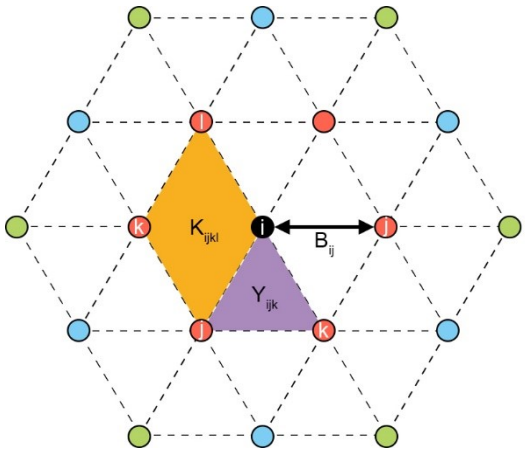

FIG. S4. Extended Heisenberg model at the atomic lattice of V layer. Higher-order exchange interactions involving the pair-wise biquadratic exchange B_{ij}, four-site four-spin exchange K_{ijkl} including electron hopping over the four lattice sites *ijkl*, and three-site four-spin exchange Y_{ijk} containing electron hopping over the three lattice sites *ijk* are indicated by the black arrow, a diamond shape in orange and a triangle in purple, respectively.

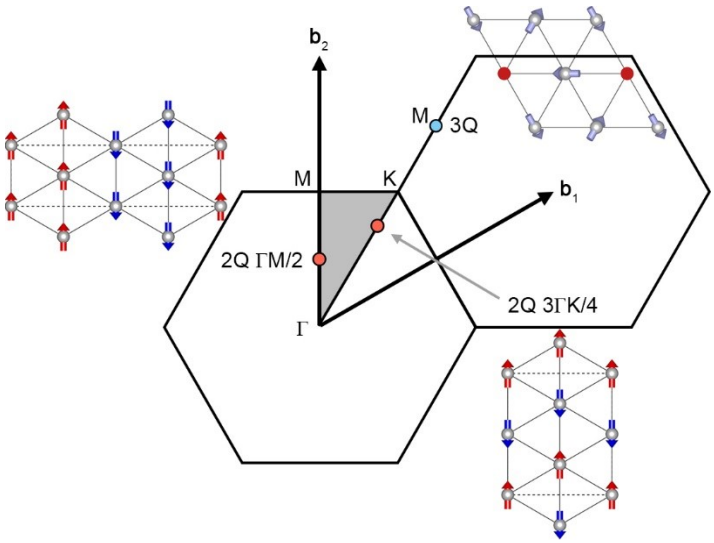

FIG. S5. Sketch of the two-dimensional hexagonal Brillouin zone with the position of ***q*** vector and the magnetic order of the two-dimensional collinear uudd spin spirals at q=ΓM/2 and q=3ΓK/4, as well as the three-dimensional noncollinear 3Q spin spirals. Note only the relative orientation of the moments in 3Q state is specified due to the neglect of the spin-orbit coupling.

Table S1. The comparison of nearest neighbor higher-order exchange parameters obtained by angular-depended and multi-Q states calculations.

System	B_1 by θ	B_1 by Q	K_1 by Q	Y_1 by Q
VSe_2	3.16	3.31	1.12	1.03
Li-VSe_2	3.59	3.09	1.04	0.39

VSe_2/Ca_2N	4.37	4.00	1.04	0.19

S4. Correlation effect of Hubbard-*U*

To determine the Hubbard-*U* of 1*T*-VSe_2 monolayer, we first calculate *U* using the linear response method of Cococcioni et al.[5] A 3×3×1 supercell of 1*T*-VSe_2 monolayer is used. The relevant response functions are found from a linear fit of the number of *d*-electrons on V site $N_{V\text{-}3d}$ in the self-consistent (SCF) and nonself-consistent (NSCF) calculations as a function of the additional potential V_{add}. The response function is defined as

$$\chi_{ij} = \frac{\partial N_i}{\partial V_j}, \tag{S6}$$

with the change in the number of *d*-electrons on site *i* due to an additional spherical potential acting on the *d*-manifold on site *j*. In the following we will assume this response to be zero unless *i*=*j*. The *U* parameter can be found from

$$U = \chi^{-1} - \chi_0^{-1} \approx \left(\frac{\partial N_i^{\mathrm{SCF}}}{\partial V_i} \right)^{-1} - \left(\frac{\partial N_i^{\mathrm{NSCF}}}{\partial V_i} \right)^{-1}. \tag{S7}$$

We obtain that χ=0.15 and χ_0=1.41, thus *U*=5.96 eV from the linear response method, as shown in Fig. S6.

Note that the *U* parameter from the linear response method is the upper limit for the DFT+*U* treatment.[6] We next compare the structural and magnetic properties using GGA-PBE functional with different *U* parameters[7,8] and hybrid functionals (HSE06). As shown in Table S2, In the DFT+*U* calculations, the lattice constant of 1*T*-VSe_2 monolayer increases as *U* parameter increases, while the magnetic ground state changes from FM to RW-AFM state when *U*>4 eV. The HSE06 calculation shows that the lattice constant of 1*T*-VSe_2 monolayer is 3.41 Å with the FM ground state. Thus, *U*=1 eV is chosen for 1*T*-VSe_2 monolayer as revealed by a linear response method and comparison with the results of HSE06.

We also compare the magnetic properties of Li-VSe_2 and VSe_2/Ca_2N using GGA-PBE functional with different U parameters and HSE06, as shown in Table S3. In the DFT+U calculations, the V atomic magnetic moment of both Li-VSe_2 and VSe_2/Ca_2N increases as U parameter increases, while the magnetic ground state changes from RW-AFM to FM state when U>1.77 eV. The HSE06 calculation shows that the ground state of both Li-VSe_2 and VSe_2/Ca_2N is RW-AFM state, which is consistent with the result of a relatively small U parameter in the DFT+U calculations. Thus, U=1 eV is chosen for both Li-VSe_2 and VSe_2/Ca_2N systems.

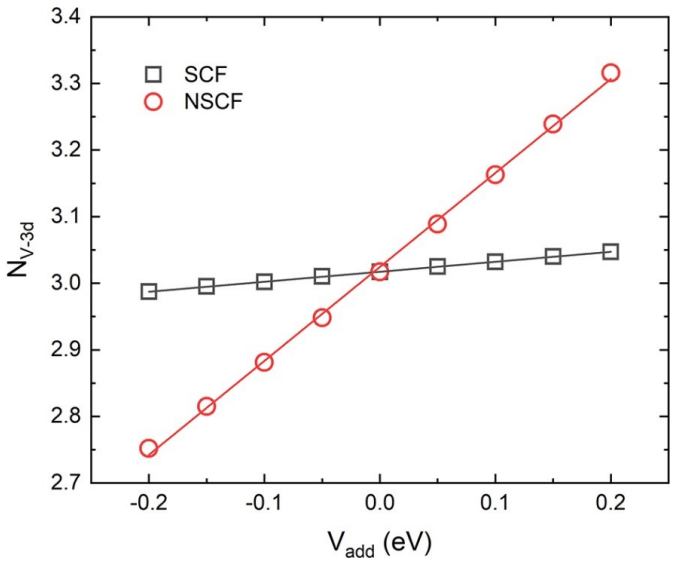

Fig. S6. $N_{V\text{-}3d}$ as a function of V_{add} for 1T-VSe_2 monolayer.

Table S2. Lattice constant a (Å), bond length of V-Se bond $l_{V\text{-}Se}$ (Å), magnetic moment of the unit cell m_{cell} (μ_B), its contributions from the V m_V (μ_B) and Se atoms m_{Se} (μ_B), and energy difference between collinear FM and RW-AFM states $E_{RW\text{-}AFM}$-E_{FM} (meV/V atom) for 1T-VSe_2 monolayer using different exchange-correlation functionals.

Functional	Hubbard-U	a	$l_{V\text{-}Se}$	m_{cell}	m_V	m_{Se}	$E_{RW\text{-}AFM}$-E_{FM}

	0	3.344	2.494	0.630	0.668	-0.045	22.182
	1	3.419	2.512	1.074	1.267	-0.124	34.180
	1.77	3.431	2.522	1.092	1.388	-0.161	13.128
GGA-PBE	3	3.490	2.534	1.068	1.397	-0.162	19.361
	4	3.539	2.547	1.023	1.424	-0.179	17.148
	4.7	3.571	2.556	1.001	1.465	-0.195	-101.716
	5.96	3.651	2.583	1.000	1.672	-0.255	-118.236
HSE06	-	3.411	2.498	1.062	1.536	-0.220	81.180

Table S3. Magnetic moment of the unit cell m_{cell} (μ_B), its contributions from the V m_V (μ_B) and Se atoms m_{Se} (μ_B), and energy difference between collinear FM and RW-AFM states $E_{RW\text{-}AFM}$-E_{FM} (meV/V atom) for Li-VSe_2 and VSe_2/Ca_2N using different exchange-correlation functionals.

System	Functional	Hubbard-U	m_{cell}	m_V	m_{Se1}	m_{Se2}	$E_{RW\text{-}AFM}$-E_{FM}
Li-VSe_2	GGA-PBE	1	1.978	1.837	-0.122	-0.082	-20.782
		1.77	2.008	1.917	-0.137	-0.087	-0.443
		3	2.001	1.997	-0.124	-0.032	69.075
	HSE06	-	2.001	1.931	-0.099	-0.016	-1.808
VSe_2/Ca_2N	GGA-PBE	1	1.695	1.731	-0.096	-0.121	-38.705
		1.77	1.747	1.829	-0.101	-0.136	-0.393
		3	1.813	1.946	-0.093	-0.145	99.980
	HSE06	-	1.722	1.903	-0.091	-0.128	-5.542

S5. Shape anisotropy

The shape anisotropy energy E_{dipole} derived from long-range magnetic dipole-dipole interactions is calculated by:

$$E_{\text{dipole}} = -\frac{1}{2}\frac{\mu_0}{4\pi}\sum_{\langle i,j\rangle}\frac{1}{\boldsymbol{R}_{ij}^3}\left[\boldsymbol{M}_i\cdot\boldsymbol{M}_j - \frac{3}{\boldsymbol{R}_{ij}^2}\left(\boldsymbol{M}_i\cdot\boldsymbol{R}_{ij}\right)\left(\boldsymbol{M}_j\cdot\boldsymbol{R}_{ij}\right)\right], \tag{S8}$$

where μ_0 is the vacuum permeability. The range of R_{max}=1000 Å is expanded to ensure the reliability since the shape anisotropy energy converges very slowly with respect to the cutoff of R_{ij}. As shown below, the calculated critical temperature of VSe_2-based systems changes within 2% after considering dipole-dipole interactions. Since the E_{dipole} is proportional to the M^2 of V atom (M~1 μ_B), the effect of dipole-dipole interactions is small that can be ignored.

Table S4. Shape anisotropy energy E_{dipole} (meV) of VSe_2-based systems.

System	E_{dipole}
pristine VSe_2	-0.03
0.2 hole doped VSe_2	-0.02
0.1 hole doped VSe_2	-0.02
0.1 electron doped VSe_2	-0.03
0.2 electron doped VSe_2	-0.03
Li-VSe_2	-0.06
VSe_2/Ca_2N	-0.05

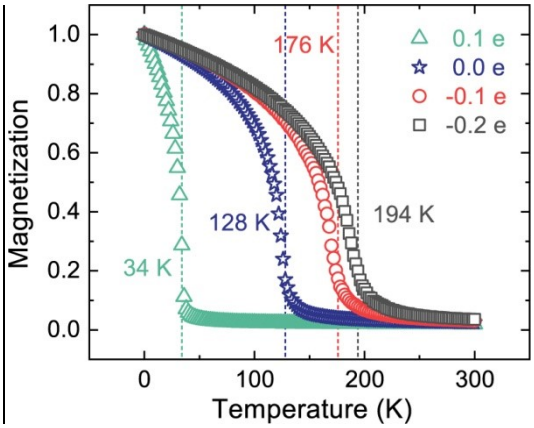

FIG. S7. Magnetization of hole/electron doped VSe_2 systems as a function of temperature. The spin model includes $J_{1\sim3}$+B_1+K+dipole.

S6. 2D-XY model

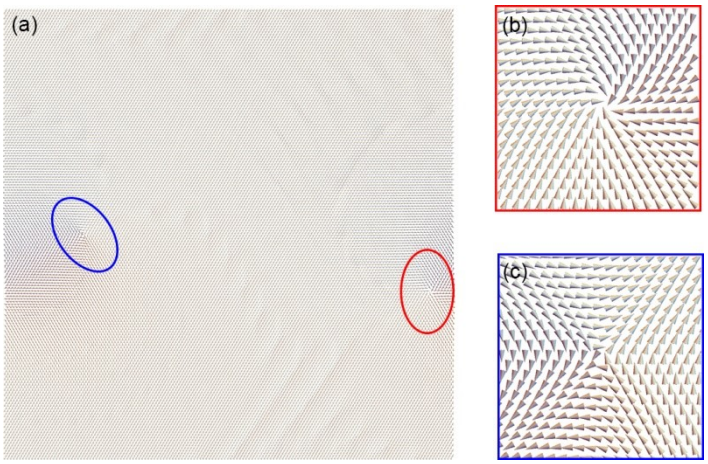

FIG. S8. (a) Real-space magnetic moments of 1*T*-VSe_2 monolayer from Monte Carlo simulations using XY model. (b) Enlarged views of a vortex in the red oval area from (a). (c) Enlarged views of a antivortex in the blue oval area from (a).

S7. Magnetocrystalline anisotropy of VSe_2 with charge doping

From the atomic resolved contribution, Se atoms dominate the in-plane magnetocrystalline anisotropy (IMA) in VSe_2 systems with charge doping, while the contribution of V atom is negligible, as shown in Fig. S9. The contribution of Se atoms increases with the valance electron number of VSe_2 systems. Moreover, a comparative analysis of MAE from orbital hybridization is performed to further elucidate the mechanism of MAE change, as shown in Fig. S10. For pristine VSe_2, the hybridization between p_y and p_x orbitals dominates the in-plane anisotropy. With the increasement of valance electron number, the contribution to IMA from p_y and p_x hybridization continuously increases, which leads to the enhancement of IMA in VSe_2. According to the second-order perturbation theory,[9] the magnetocrystalline anisotropy energy (MAE) can be expressed as:

$$\mathrm{MAE} = \xi^2 \sum_{\sigma\sigma'} \sum_{o^{\sigma}, u^{\sigma'}} \frac{(2\delta_{\sigma\sigma'} - 1)\left(\left|\left\langle o^{\sigma} \left| L_z \right| u^{\sigma'} \right\rangle\right|^2 - \left|\left\langle o^{\sigma} \left| L_x \right| u^{\sigma'} \right\rangle\right|^2\right)}{E_u^{\sigma'} - E_o^{\sigma}}, \tag{S9}$$

where ξ is the spin-orbit coupling amplitude. $E_u^{\sigma'}$ and E_o^{σ} are the energy levels of unoccupied states with spin σ' and occupied states with spin σ, respectively. $(2\delta_{\sigma\sigma'} - 1)\left(\left|\left\langle o^{\sigma} \left| L_z \right| u^{\sigma'} \right\rangle\right|^2 - \left|\left\langle o^{\sigma} \left| L_x \right| u^{\sigma'} \right\rangle\right|^2\right)$ is the difference of spin-orbital angular momentum matrix elements shown in Table S4. From the projected density of states (DOS) of Se-*p* orbitals in VSe_2 with charge doping, it is clear that the p_y and p_x orbitals are almost degenerated. Furthermore, with the increasement of valance electron number, the occupied spin-down p_y/p_x ($p_y^{o^-}/p_x^{o^-}$) state is shifted to the Fermi level, and the unoccupied spin-up p_y/p_x ($p_y^{u^+}/p_x^{u^+}$) state is shifted to the higher level above the Fermi level, leading to the reduction of $E_u^{\sigma'} - E_o^{\sigma}$. As shown in Table S5, since the matrix elements difference between $p_y^{u^+}$ and $p_x^{o^-}$ (or $p_x^{u^+}$ and $p_y^{o^-}$) is -1, the negative MAE from p_y and p_x hybridization is enhanced.

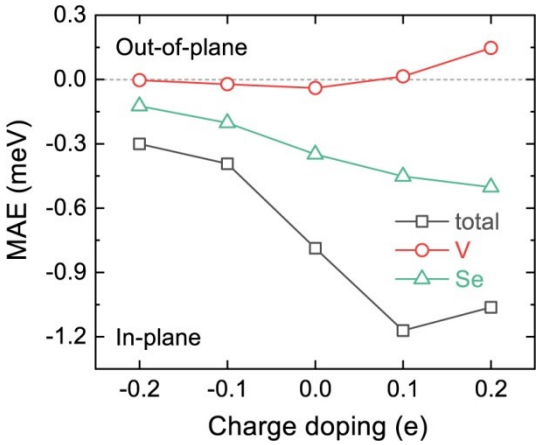

FIG. S9. Calculated MAE of VSe_2 with charge doping and its atomic resolved contribution.

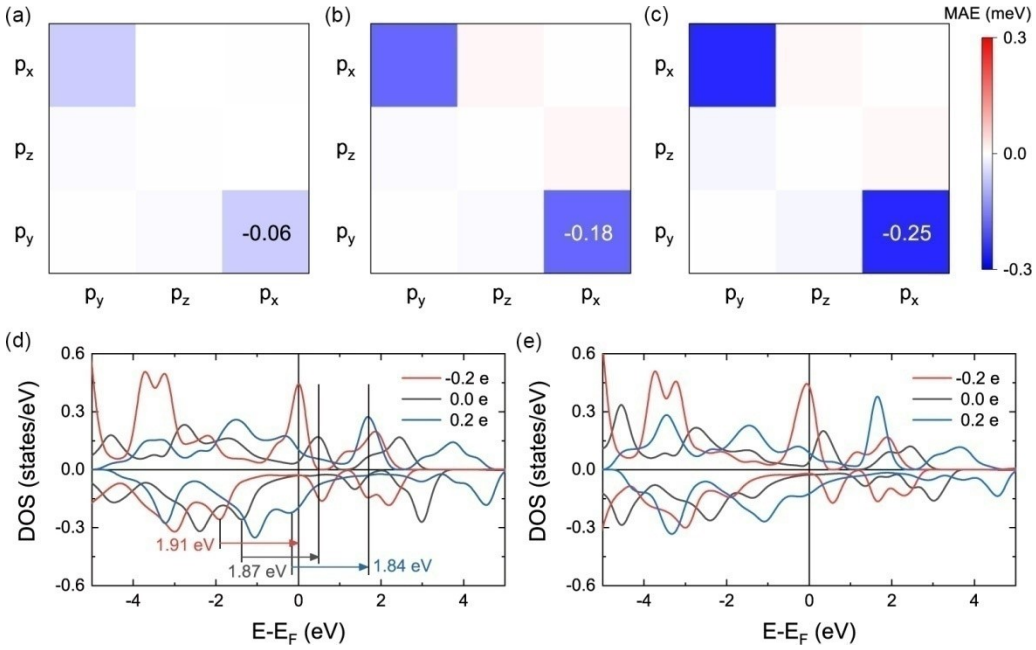

FIG. S10. Contributions to MAE from Se-*p* orbitals hybridization of (a) 0.2 hole doped, (b) pristine and (c) 0.2 electron doped VSe_2. DOS of (d) Se-p_y and (e) Se-p_x orbitals in VSe_2 with charge doping.

Table S5. Matrix differences between magnetization along out-of-plane [001] and in-plane direction [100]. The u^+,

o^- and o^+ represent the unoccupied spin-up, occupied spin-down and occupied spin-up states, respectively.

u^+	o^-			o^+		
	p_y	p_z	p_x	p_y	p_z	p_x
p_y	0	1	-1	0	-1	1
p_z	1	0	0	-1	0	0
p_x	-1	0	0	1	0	0

S8. Adsorption configurations and stability of Li-VSe_2, as well as stacking configurations and van der Waals correction methods of VSe_2/Ca_2N bilayer

In Fig. S11, the most stable adsorption configurations of Li-VSe_2 are investigated. Three considered adsorption sites are Li atom on the top of V, Se1 and Se2 atoms, which are labeled as Li-1, Li-2, and Li-3, respectively. Among them, Li-1 is the most energetically favorable one, in which the total energies of Li-2 and Li-3 are 0.14 and 0.60 eV higher than that of Li-1.

The most stable stacking configurations of VSe_2/Ca_2N bilayer are investigated. Six possible stacking configurations are labeled as m-1 to m-6. Among them, m-6 is the most energetically favorable one, in which the total energies of m-1, m-2, m-3, m-4 and m-5 are 0.06, 0.60, 0.08, 0.59 and 0.15 eV higher than that of m-6.

Ab initio molecular dynamics simulations with the constant-volume constant-temperature (NVT) ensemble and a time step of 2 fs are performed to confirm the thermal stability of Li-VSe_2 at 300 K. The system displays small energy fluctuations across the simulation, as shown in Fig. S12. The inset shows the snapshot of Li-VSe_2 after 6 ps, where neither structural reconstruction nor broken bonds are present, which demonstrates that Li-VSe_2 is thermally stable. The $LiVS_2$, $LiCrS_2$ and $NaCrS_2$ have been prepared and can be cleaved from the bulk form,[10,11] which suggests the possible stability of monolayer $LiVSe_2$. Moreover, the Li-ion adsorption concentration indeed has influence on the magnetism of VSe_2, and our main goal is to investigate the effect of Li adsorption on the magnetic interaction of VSe_2. We also calculate the magnetic ground state of Li-ion doped VSe_2 with lower doping concentration, e.g., $Li_{1/3}VSe_2$ and $Li_{2/3}VSe_2$, as shown in Fig. S13. According to the Bader charge analysis, there are ~0.29 and 0.57 electrons transferred to the VSe_2 layer. The RW-AFM states are more favorable with energy difference of -34.77 and -43.49 meV per

V atom lower than FM states for $Li_{1/3}VSe_2$ and $Li_{2/3}VSe_2$, respectively, which is consistent with the results of our valence electron model.

In order to analysis the bonding type between VSe_2 and Ca_2N in VSe_2/Ca_2N bilayer, the calculated electron localization function (ELF) is shown in Fig. S14. Obviously, an electron gas with an ELF value of ~0.44 exists on the side of the Ca_2N layer away from the interface, while the electron gas at the interface disappears, indicating that the electron is transferred to the VSe_2 layer. In addition, the ELFs of the Ca2 and Se1 sites at the interface are around 0.52 and 0.75, respectively. In the middle of Ca2-Se1 bond (2.98 Å bond length), the electrons are completely delocalized, suggesting that the binding of Ca2 and Se1 deviates from the vdW behavior and is more similar to an ionic bond. Different vdW correction methods are used to compare the interlayer distances, magnetic moment and energy difference between collinear FM and RW-AFM states, as shown in Table S6. The interlayer distance is in the range of 2.17–2.28 Å with no significant change in the magnetic moment and energy difference, both without correction and with the selected correction methods, which shows the rationality of the D3 method in calculating VSe_2/Ca_2N bilayers.

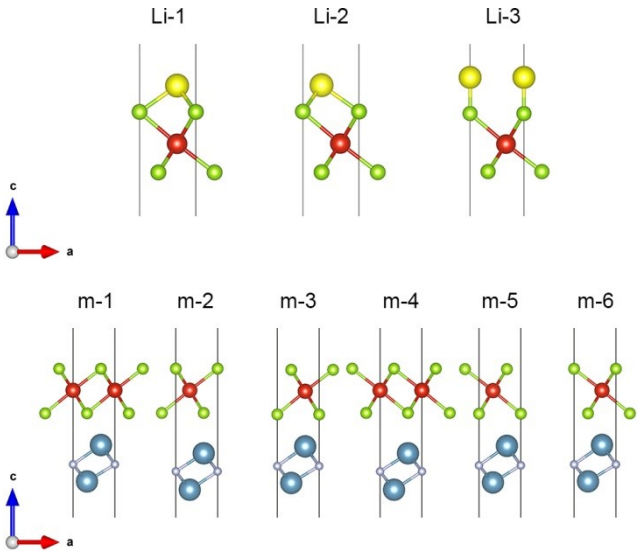

FIG. S11. Side views of geometric structures for (a) Li-VSe_2 monolayer with different adsorption sites and (b) VSe_2/Ca_2N bilayer with different stacking configurations.

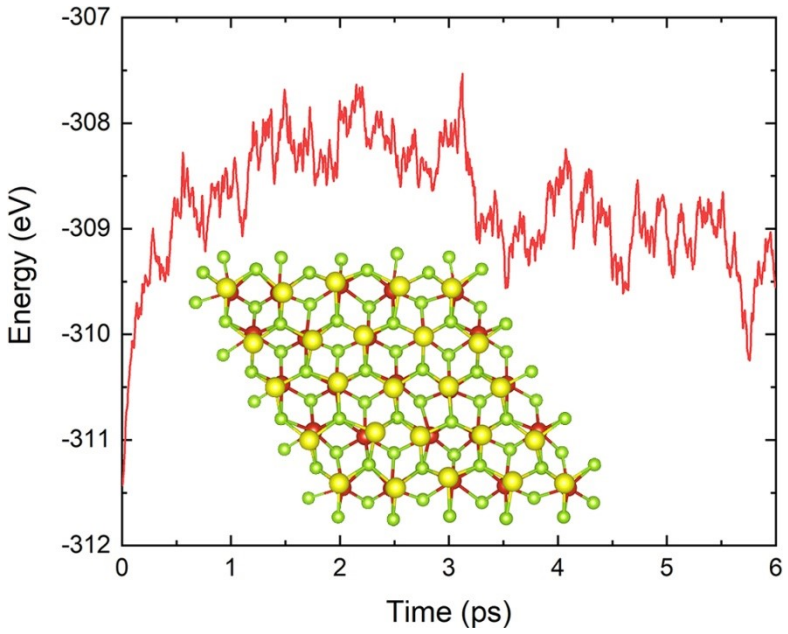

Fig. S12. Variation of the total energy as a function of the simulation time in the AIMD simulation at 300 K. The inset is the top view of the geometrical structure of Li-VSe_2 supercell at 6 ps.

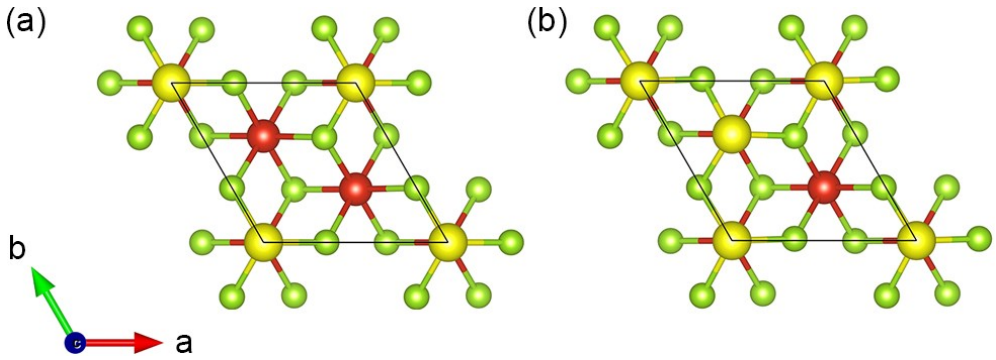

Fig. S13. Geometric structures of (a) $Li_{1/3}VSe_2$ and (b) $Li_{2/3}VSe_2$. The unit cell is shown by black solid lines.

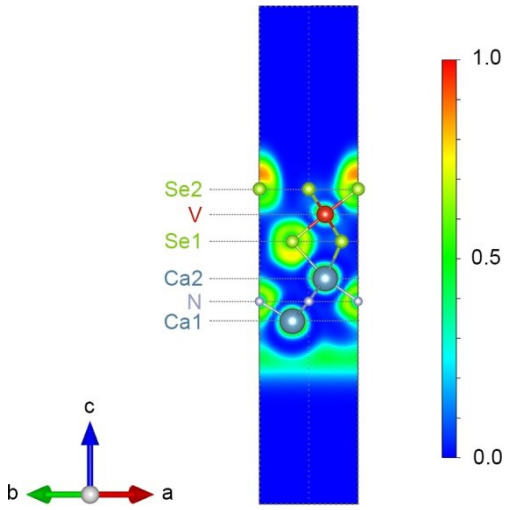

Fig. S14. Electron localization function of VSe_2/Ca_2N bilayer.

Table S6. Dependence of the optimized interlayer distances d (Å), magnetic moment of the unit cell m_{cell} (μ_B) and energy difference between collinear FM and RW-AFM states $E_{RW\text{-}AFM}$-E_{FM} (meV/V atom) of VSe_2/Ca_2N on the methods of van der Waals correction.

Methods	No correction	D2[a]	D3[b]	D3-BJ[c]	TS[d]	TS-H[e]	dDsC[f]
d	2.277	2.281	2.232	2.213	2.170	2.234	2.245
m_{cell}	1.690	1.690	1.695	1.694	1.696	1.694	1.694
$E_{RW\text{-}AFM}$-E_{FM}	-37.032	-40.154	-38.705	-39.496	-44.900	-39.107	-38.120

[a]DFT-D2 method,[12] [b]Zero-damping variant of the DFT-D3 method,[13] [c]Becke-Johnson (BJ) damping variant of the DFT-D3 method,[13,14] [d]Tkatchenko-Scheffler (TS) method,[15] [e]TS method with iterative Hirshfeld partitioning,[16] [f]DDsC dispersion correction[17,18]

S9. Magnetocrystalline anisotropy of Li-VSe_2 and VSe_2/Ca_2N

The angular depended magnetocrystalline anisotropy energy of Li-VSe_2 and VSe_2/Ca_2N is also calculated, as shown in Fig. S15. The lowest energy occurs at θ=0 in the *xz* plane, while the energy difference is negligible in the *xy* plane, which means that both Li-VSe_2 and VSe_2/Ca_2N exhibit an easy magnetization plane. Corresponding to the analysis of the valence electron number model, Se atoms have the most contribution to IMA of Li-VSe_2 and VSe_2/Ca_2N systems from the atomic resolved MAE, as shown in Fig. S16. Note that in Li-VSe_2 system, Se1 dominates the IMA, in which Se2 has a relatively small negative value. Additionally, the p_y and p_x orbitals in Se atoms of both Li-VSe_2 and VSe_2/Ca_2N show obvious hybridization, resulting in the enhancement of IMA, as shown in Fig. S17.

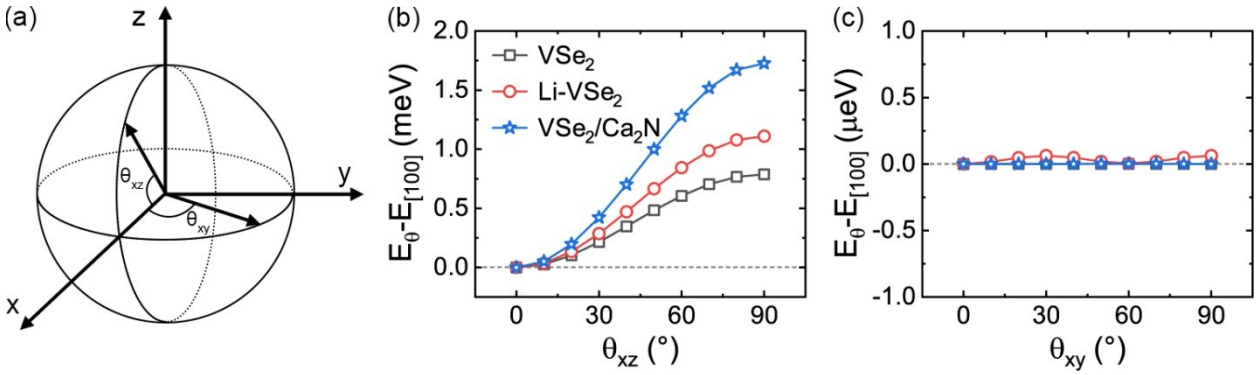

Fig. S15. (a) Diagram of magnetic moments arranged in different directions. Angular depended magnetocrystalline anisotropy energy of VSe_2, Li-VSe_2 and VSe_2/Ca_2N in (b) *xz* plane and (c) *xy* plane.

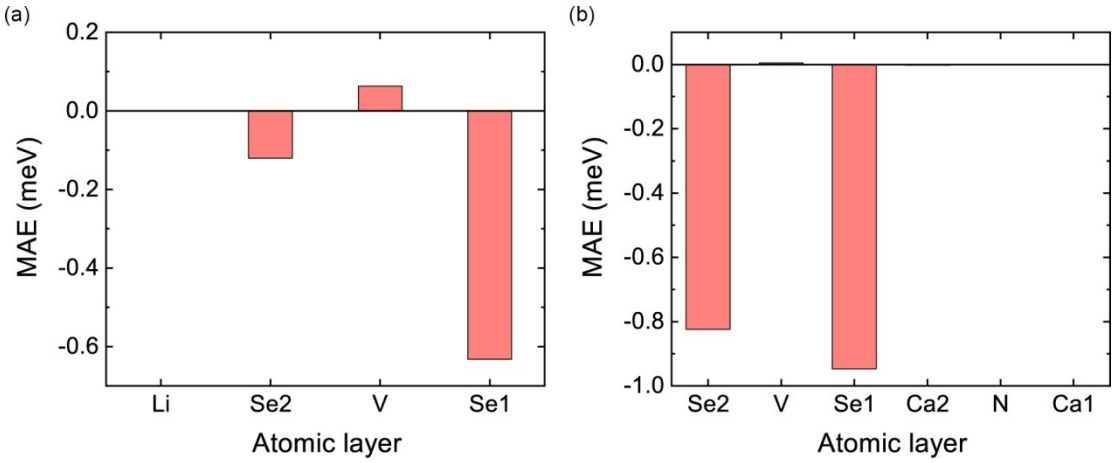

FIG. S16. Atomic resolved MAE of (a) Li-VSe_2 and (b) VSe_2/Ca_2N.

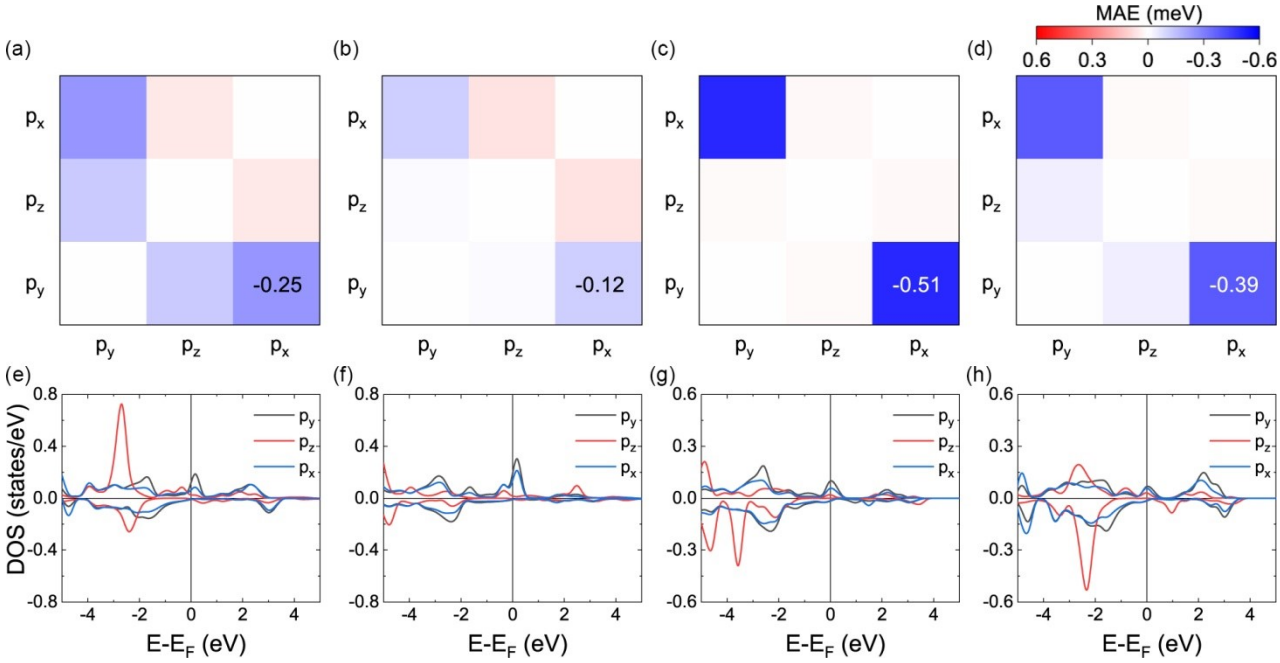

FIG. S17. Contributions to MAE from Se-*p* orbitals hybridization of (a) Se1 in Li-VSe_2, (b) Se2 in Li-VSe_2, (c) Se1 in VSe_2/Ca_2N and (d) Se2 in VSe_2/Ca_2N. DOS of (e) Se1-*p* orbitals in Li-VSe_2, (f) Se2-*p* orbitals in Li-VSe_2, (g) Se1-*p* orbitals in VSe_2/Ca_2N and (h) Se2-*p* orbitals in VSe_2/Ca_2N.

References

1 J. Spethmann, S. Meyer, K. von Bergmann, R. Wiesendanger, S. Heinze, and A. Kubetzka, Discovery of magnetic single- and triple-q states in Mn/Re(0001), *Phys. Rev. Lett.*, 2020, **124**, 227203).

2 B. Hardrat, A. Al-Zubi, P. Ferriani, S. Blügel, G. Bihlmayer, and S. Heinze, Complex magnetism of iron monolayers on hexagonal transition metal surfaces from first principles, *Phys. Rev. B*, 2009, **79**, 094411.

3 P. Kurz, G. Bihlmayer, K. Hirai, and S. Blügel, Three-dimensional spin structure on a two-dimensional lattice: Mn/Cu(111), *Phys. Rev. Lett.*, 2001, **86**, 1106-1109.

4 M. Hoffmann and S. Blügel, Systematic derivation of realistic spin models for beyond-Heisenberg solids, *Phys. Rev. B*, 2020, **101**, 024418.

5 M. Cococcioni and S. de Gironcoli, Linear response approach to the calculation of the effective interaction parameters in the LDA+U method, *Phys. Rev. B*, 2005, **71**, 035105.

6 J.-J. Xian, C. Wang, J.-H. Nie, R. Li, M. Han, J. Lin, W.-H. Zhang, Z.-Y. Liu, Z.-M. Zhang, M.-P. Miao, Y. Yi, S. Wu, X. Chen, J. Han, Z. Xia, W. Ji, and Y.-S. Fu, Spin mapping of intralayer antiferromagnetism and field-induced spin reorientation in monolayer $CrTe_2$, *Nat. Commun.*, 2022, **13**, 257.

7 H. Sheng, H. Long, G. Zou, D. Bai, J. Zhang, and J. Wang, Magnetic and phonon transport properties of two-dimensional room-temperature ferromagnet VSe_2, *J. Mater. Sci.*, 2021, **56**, 15844-15858.

8 S. Memarzadeh, M. R. Roknabadi, M. Modarresi, A. Mogulkoc and A. N. Rudenko, Role of charge doping and strain in the stabilization of in-plane ferromagnetism in monolayer VSe_2 at

room temperature, *2D Mater.*, 2021, **8**, 035022.

9 D.-S. Wang, R. Wu, and A. J. Freeman, First-principles theory of surface magnetocrystalline anisotropy and the diatomic-pair model, *Phys. Rev. B*, 1993, **47**, 14932-14947.

10 B. van Laar and D. J. W. Ijdo, Preparation, crystal structure, and magnetic structure of $LiCrS_2$ and $LiVS_2$, *J. Solid State Chem.*, 1971, **3**, 590-595.

11 H. J. Scheel, Crystallization of sulfides from alkali polysulfide fluxes, *J. Cryst. Growth*, 1974, **24-25**, 669-673.

12 S. Grimme, Semiempirical GGA-type density functional constructed with a long-range dispersion correction, *J. Comput. Chem*., 2006, **27**, 1787-1799.

13 S. Grimme, J. Antony, S. Ehrlich, and H. Krieg, A consistent and accurate *ab initio* parametrization of density functional dispersion correction (DFT-D) for the 94 elements H-Pu, *J. Chem. Phys.*, 2010, **132**, 154104.

14 S. Grimme, S. Ehrlich, and L. Goerigk, Effect of the damping function in dispersion corrected density functional theory, *J. Comput. Chem.*, 2011, **32**, 1456-1465.

15 A. Tkatchenko and M. Scheffler, Accurate molecular van der Waals interactions from ground-state electron density and free-atom reference data, *Phys. Rev. Lett.*, 2009, **102**, 073005.

16 T. Bučko, S. Lebègue, J. Hafner, and J. G. Ángyán, Improved density dependent correction for the description of London dispersion forces, *J. Chem. Theory. Comput.*, 2013, **9**, 4293-4299.

17 S. N. Steinmann and C. Corminboeuf, A generalized-gradient approximation exchange hole model for dispersion coefficients, *J. Chem. Phys.*, 2011, **134**, 044117.

18 S. N. Steinmann and C. Corminboeuf, Comprehensive benchmarking of a density-dependent dispersion correction, *J. Chem. Theory Comput.*, 2011, **7**, 3567-3577.